Available online at www.sciencedirect.com

ScienceDirect

Journal of the European Ceramic Society 35 (2015) 2413–2425

www.elsevier.com/locate/jeurceramsoc

Three-dimensional shrinkage behavior of green tapes derived from spherical-shaped powders: Experimental studies and numerical simulations

Zongwen Fu [a], Pit Polfer [b], Torsten Kraft [b], Andreas Roosen [a,*]

[a] University of Erlangen-Nuremberg, Department of Materials Science, Glass and Ceramics, Martensstrasse 5, 91058 Erlangen, Germany
[b] Fraunhofer Institute for Mechanics of Materials IWM, Wöhlerstrasse 11, 79108 Freiburg, Germany

Received 13 August 2014; received in revised form 22 January 2015; accepted 30 January 2015
Available online 20 February 2015

Abstract

In tape-cast products a higher shrinkage is observed in the thickness direction compared to the in-plane shrinkage, which is attributed to an anisotropic green tape microstructure caused by shearing and drying during manufacturing. In the present study, cast tapes composed of spherical particles were investigated experimentally and numerically. The shrinkage behavior was analyzed after binder removal and sintering at different temperatures in all three spatial directions. The correlation between anisotropic shrinkage and microstructure concerning pore orientation and coordination number was discussed. Furthermore, it is shown that the anisotropic shrinkage during binder removal contributes strongly to the total shrinkage anisotropy.

Keywords: Tape casting; Anisotropic shrinkage; Ceramic sintering; Discrete element method; Simulation

1. Introduction

Dimensional control is one of the basic problems in ceramic processing, especially for tape cast sheets which are used to manufacture multilayer structures with highly integrated components.[1,2] In this technology, the exact positions, e.g., of vias or electrodes in different layers must be maintained during the entire thermal process.[2] Therefore, any uncontrolled shrinkage anisotropy during binder burnout and sintering can lead to device failure.[3–6] During tape casting, due to the shear flow gradient under the blade of the casting head as well as to the constrained drying process, non-spherical ceramic particles are predominantly oriented parallel to the casting direction.[7–15] Because of this anisotropic green tape microstructure, anisotropic shrinkage occurs:[8,13,14,16]

$$\varepsilon_z \gg \varepsilon_y \gg \varepsilon_x \quad (1)$$

where ε represents the linear sintering shrinkage and x, y and z denote the casting, transverse and thickness direction, respectively.

Not only tape-cast products exhibit an anisotropic microstructure; the shrinkage anisotropy could also be observed during the sintering of uniaxially pressed, extruded and three-dimensional printed ceramics.[17–19] During uniaxial pressing, extrusion and tape casting, it was found that non-spherical ceramic particles can be textured and that the largest and smallest shrinkages occur in the directions perpendicular and parallel to the particle orientation direction, respectively.[17] During rapid prototyping based on layer-by-layer assemblies via 3D printing, elongated pores perpendicular to the thickness direction as well as a layered microstructure could be found.[18,19] In all these cases a higher shrinkage in the z-direction was observed; the primary cause of anisotropic shrinkage in these systems is attributed to the orientation of anisotropic particles.[11,16,19–25] Wakai et al. simulated the shrinkage behavior of spherical particles, which are not oriented but which also exhibit anisotropic shrinkage behavior caused by particle rearrangement during sintering due to an inhomogeneous distribution of contact points.[26]

* Corresponding author. Tel.: +49 91318527540.
E-mail address: andreas.roosen@fau.de (A. Roosen).

http://dx.doi.org/10.1016/j.jeurceramsoc.2015.01.032
0955-2219/

According to the sintering theory, grain growth and pore elimination are the two most important mechanisms to describe sintering shrinkage.[27] In the present work, three-dimensional shrinkage behavior of tape cast alumina powders of spherical particle shape was investigated experimentally and numerically, and correlated with pore orientation and coordination number in the microstructure. Specifically, the reason for the higher shrinkage in z-direction compared to the lateral shrinkage is in focus. The study is based on experiments as well as on simulation of sintering behavior.

2. Experimental methods

2.1. Raw materials

Spherical alumina powders SP (Sumitomo Chemical Co., Ltd., Tokyo, Japan, $\boldsymbol{d}_{50}$: ~3.0 μm) and DAW 05 (Denka Co., Ltd., Tokyo, Japan, $\boldsymbol{d}_{50}$: ~4.2 μm) were used in the present study. The particle size distribution was measured by means of laser granulometry (Mastersizer APA 2000, Malvern Instruments, London, Great Britain).

2.2. Slurry preparation and tape casting

Tape casting slurries with a solid content of 28 vol.% alumina were prepared; powder dispersion was performed in a tumbling mixer (Turbula, Willy A. Bachofen AG, Swiss) with Al_2O_3 milling balls for 24 h in an azeotropic solvent mixture containing of 68 wt.% ethanol and 32 wt.% toluene; Menhaden Fish oil (Kellogg Co., Buffalo, USA) was added as dispersant. After 24 h of deagglomeration, binder (polyvinylbutyral, B-98, Solutia Inc., St. Louis, USA) and plasticizer (alkyl benzyl phthalate, Santicizer, Ferro Corp., Cleveland, USA) were added to the suspension. Subsequently, the slurry was homogenized for an additional 24 h, sieved through a 200 μm mesh screen and degassed (250 mbar, 30 min) to remove gas bubbles before casting. Table 1 shows the exact composition of the tape casting slurry used in this study and also the density of the components.

Tape casting was carried out on a tape-casting machine equipped with a fixed double-chamber casting head. A silicon-coated PET carrier film (Mitsubischi Plastics, Inc., Japan) with a thickness of ~100 μm was used as a tape carrier. The front and rear doctor blades were adjusted to a gap height of 900 μm and 1100 μm, respectively. Because increasing shear rates above ~12 s^{-1} did not result in an increased particle alignment,[8,12] the casting speed was kept at a constant value of 700 mm/min in this study. The filling height of the slurry reservoir was ~20 mm in all cases. Drying was performed at room temperature without additional air flow.

2.3. Sample preparation

The dried green sheets with a thickness between 240 and 280 μm, respectively, were removed from the PET carrier film and cut to the desired sample size of 30 mm × 30 mm with a hot knife (Groz-Beckert KG, Albstadt, Germany) at 60 °C. Debinding took place in air with a heating rate of 2 K/min up to 450 °C, followed by a holding time of 1 h. Subsequently, the samples were pre-fired at 1600 °C in air with a holding time of 1 h and a heating rate of 4 K/min on a high purity alumina setter (Kerafol GmbH, Eschenbach, Germany). In order to improve the densification, the pre-fired tapes were subsequently sintered at 1600 °C for 10 h as well as at 1730 °C for 5 h and for 15 h, respectively. Due to plastic deformation of alumina setter at these higher temperatures, porous mullite substrates were used as sintering support during these sintering experiments. The theoretical density of ceramic tapes before and after firing was calculated using the theoretical density values shown in Table 1. The bulk density of green tapes was determined by measuring the weight, the area by scanning of the surface geometry using a commercial scanner (Epson Perfection V500 PHOTO, Epson GmbH, Meerbusch, Germany, resolution: ~22 μm/pixel) and the height by means of micrometer screw. The bulk density after BBO and sintering was calculated according to mass loss and to measured shrinkage by laser scanning microscopy. The porosity was derived from the measured bulk and theoretical densities.

2.4. Analysis of shrinkage anisotropy

In order to determine the shrinkage anisotropy, the linear shrinkage in all three spatial directions was measured. For the measurement of the shrinkage in the casting plane, four hardness indentations in a distance of ~25 mm from each other were punched into the green tapes using a Vickers diamond pyramid (Zwick GmbH & Co. KG, Ulm, Germany).[8] The exact distance between these indentations was measured before and after firing by means of a laser scanning microscopy (UBM Messtechnik GmbH, Ettlingen, Germany) with an accuracy of 10 nm in z-direction and 1 μm in $\boldsymbol{x}$- and $\boldsymbol{y}$-directions. In order to measure the thickness shrinkage exactly, the average thickness along the two diagonals of small, non-warped specimens of about 1 mm × 1 mm in size was determined by means of laser scanning microscopy before and after debinding and pre-firing. The use of these two methods allowed an exact measurement of the shrinkage in all three spatial directions. Furthermore, the thickness before and after sintering was verified by micrometer screw gauge with an accuracy of 1 μm. Due to the relatively high surface roughness of the porous mullite setters used for sintering at higher temperatures above 1600 °C and holding times of 10 h, the beam of the laser scanning microscope was out of the measuring range of ± 500 μm. Therefore, the thickness had to be determined by micrometer screw gauge.

Average values of the shrinkage were calculated from measurements of at least ten different samples. Based on these data, the shrinkage anisotropy factors $\boldsymbol{K}$ in all three spatial directions were calculated according to the following equations:

$$\boldsymbol{K}_{xy} = \left(1 - \frac{\boldsymbol{\varepsilon}_x}{\boldsymbol{\varepsilon}_y}\right) \times 100 \quad (2)$$

$$\boldsymbol{K}_{xz} = \left(1 - \frac{\boldsymbol{\varepsilon}_x}{\boldsymbol{\varepsilon}_z}\right) \times 100 \quad (3)$$

Table 1
Composition of the Al_2O_3 slurries used.

	Volume fraction in the slurry [vol.%]	Weight fraction in the slurry [wt.%]		Density [g/cm^3]	
		SP	DAW 05	SP	DAW 05
Al_2O_3 powder	28.00	63.87	62.30	3.970**	3.722**
Solvent (68 wt.% ethanol + 32 wt.% toluene)	54.92	25.65	26.77	0.815*	
Dispersant	2.25	1.28	1.34	0.993*	
Binder	7.50	4.73	4.93	1.100*	
Plasticizer	7.33	4.47	4.66	1.063*	

* Density given by producer.
** Measured by helium pycnometry.

$$K_{yz} = \left(1 - \frac{\varepsilon_y}{\varepsilon_z}\right) \times 100 \quad (4)$$

where ε represents the linear sintering shrinkage and x, y and z denote the casting, transverse and thickness direction, respectively.

2.5. Microstructure analysis

In order to characterize pore and particle orientation in the alumina tapes, the microstructure of the cross sections in the xy-, xz- and yz-planes was analyzed by scanning electron microscopy (SEM, Quanta 200, FEI Ltd, Hillsboro, OR, USA). For that purpose the samples were polished with a 1 μm diamond finish and sputtered with gold. Because the mechanical strength of the green tapes was not sufficient for the preparation of polished cross sections, the microstructure analysis was performed on samples after different thermal treatments at temperatures of 1600 and 1730 °C. For image analysis, all SEM micrographs were converted into binary pictures using "ImageJ" (National Institutes of Health, Bethesda, Maryland, USA). Picture size and resolution were adjusted to 643 pixel × 643 pixel with 0.149 μm/pixel, respectively. The porosity P in each cross section was determined by calculating the area fraction of pores.

2.5.1. Modified linear intercept method

In order to determine the orientation degree of irregular pores, the modified linear intercept method was used in the present study; details of this method are described in.[16] The micrograph is covered with a horizontal and vertical grid lines, and the cumulative pore space number is measured along each grid line in both directions, respectively. The pore orientation factor S is defined by the following equation:[16,28]

$$S_{xy} = \left(1 - \frac{N_x}{N_y}\right) \times 100 \quad (5)$$

where N denotes the cumulative number of pore spaces on every straight grid line. The factor S_{xy} is greater than zero when pores are oriented in x-direction. With increasing texture the S-value can be significantly enhanced. The pore anisotropy factor S in other spatial planes can be calculated accordingly. In this study due to the spherical particle shape, the particle anisotropy factor is nearly 0 and therefore it was not determined.

Furthermore, to get results of high resolution from the image analysis, the grid distance between two neighboring intercept lines was adjusted to zero, meaning that SEM pictures were analyzed pixel by pixel applying an own evaluation software. Details of the methodology are given in.[16] Average S values were calculated from at least four measurements by analyzing cross sections with more than 100,000 pore spaces.

3. Simulation method

The goal of the simulation is to investigate the influence of the different process steps on the shrinkage behavior depending on the geometrical arrangement of the particles prior to sintering. One important difference between the simulation and the experiments is that the binder burnout is not taken into account in the simulation, which will lead to a substantial difference between the numerical and the experimental results. The importance of binder burnout on shrinkage behavior of green tapes was already published.[37] Since the following numerical investigations do not intend to exactly reproduce the experiments quantitatively but should aid in understanding the mechanisms taking place at particle level during the different process steps, this simplification is justified.

To achieve this, a simulation scheme was set-up which includes the major physical mechanisms occurring during the whole process chain. Some simplifications in the modeling had been necessary in order to be computationally manageable in a finite time frame. However, it was ensured that the number of simulated ceramic particles was large enough in order to ensure realistic behavior. The method used for all three process steps is the discrete element method (DEM).[29] This method allows for the simulation of the ceramic particles without explicitly modeling the fluid phase, a simplification which highly reduces the computational effort. Besides this it offers the advantage of having been applied to a vast number of different applications including the simulation of suspensions, drying and the sintering of ceramics.[30,31]

The simulations in this study can be divided in three different parts. The first part is the simulation of the tape casting process, mainly of what is happening at the particle scale during the passage of the ceramic suspension under the doctor blade. The second part is the drying process where the initial particle setup is the result of the aforementioned tape casting. Additionally, drying simulations are also performed with the original initial particle setups prior to the tape casting simulation in order to analyze the influence of the shear strain on the drying behavior.

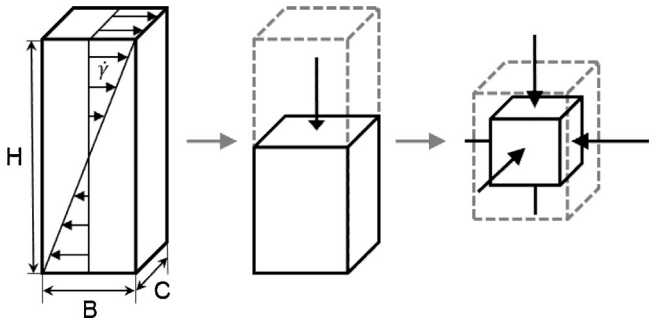

Fig. 1. Scheme of the simulation principle of the three process steps, from left to right: tape casting (shear under the blade), drying and sintering.

Finally, the results of the drying simulations are used to feed the sintering simulations (Fig. 1).

Two different idealized powders were used in the numerical study. Both consist of spherical particles. One powder consists of equally sized particles (hereafter named ESP), whereas the other powder has particles with a log-normal size distribution (hereafter named PSD). For each powder six different starting setups with random particle position were generated in order to get some information on statistical variations of initial positions. In all, it results in 12 initial setups. The particle radius is set to 2.1 μm and in case of the particle size distribution the log-normal distribution parameter σ is set to 0.15. The distribution is narrower than in the experiments due to the fact that large particle size differences result in a disproportional increase of the computational effort. Nevertheless, for qualitative investigations of the influence of the particle size distribution this simplification is regarded as acceptable.

The initial setup consists of a 3d box with the dimensions $270 \times 80 \times 80$ μm ($H \times B \times C$ in Fig. 1). Depending on the powder the setups consist of between 11,600 and 13,000 DEM particles. This results in a solids loading of the slurry of 29 vol.%. Furthermore, gravity has not been taken into account since this simplification will lead to more specific results regarding the influence of the processing steps on the sintering behavior. Finally, the suspension is regarded as being stabilized.

3.1. Simulation of tape casting

The simulation of the slurry movement underneath the doctor blade during the tape casting process focuses on the movement and interaction of the ceramic particles. The goal of this simulation is to determine the influence of the shear field under the blade on the particle packing and to investigate to which extend an ordered particle arrangement develops during this process step.

These DEM simulations consist of a 3d box with Lees-Edwards boundary conditions.[32] The Stokes drag is applied in respect to the Couette flow field in the box. Each setup was sheared for 0.18 s with a shear rate of 111.1 s^{-1}. The viscous dampening is included through the Stokes drag law and has been set to the viscosity of the solvent including additives and binder (0.42 Pa s).[9] This reduces the simulation cost as solvent, additives and binder do not need to be explicitly modeled. The interactions between the particles are governed by the Hertzian repulsion and the Coulomb friction law.[29] No other forces between particles have been taken into account as both, the steric repulsion and the van-der-Waals attraction, have very small ranges compared to the particle radii used in this study.[33]

3.2. Simulation of the drying process

The final particle positions from the casting simulations are used as input for the drying simulations. Additionally, for each setup the drying is simulated with the initial particle positions taken prior to tape casting to identify the influence of the shearing on the subsequent drying process resulting in a total of 24 drying simulations. Only the first drying phase, or constant rate phase,[34] is simulated since later on less significant rearrangement processes are expected due to the close packing of the particle and the gluing effect of the organic binder when most of the solvent is already evaporated. The DEM model used for this drying process is described in.[30] The effect of any horizontal capillary force is neglected since the main focus of this study is on the packing of the particles in the bulk. Similar to,[30] the position of the interface between the air and the fluid over time is given by a linear analytical function. Particles at the interface are subject to the vertical capillary force and interactions are governed by the same laws as in the tape casting simulation. Again, a Stokes drag law has been used to include the effects of the solvent on the ceramic particles.

Triggered by the computational demands a higher drying rate than applied experimentally is used. The simulation is stopped as soon as the drying interface is entering the network of ceramic particles as discussed in detail above. Additionally, the particle size and the background viscosity have been adjusted to further reduce the computation time. All this has been done while keeping the Reynolds number less than unity in order to preserve the fundamental behavior of the system.

This methodology to study the drying process together with the parametric studies shown later prepares the basis for a better understanding of the particle ordering depending on either the casting conditions or during the subsequent drying step as well as the general influence of drying on particle packing before sintering. It should also be noted that the binder burnout is not taken into account in the simulation.

3.3. Simulation of the sintering process

The DEM sintering model used in this paper has been developed for solid state sintering[31] and has been applied several times to the sintering of alumina powders, e.g.[35,36] Since the sintering simulations are used only for qualitative investigations the model parameters for the powders had not been determined in detail. Instead, existing data of an alumina powder have been used[36] and the systems were scaled to conform to the properties of the aforementioned study.

The initial setups for the sintering simulation are provided by the 24 drying simulations. The setups of the dried tapes are cropped at the surface and near the substrate in order to reduce the influence of these interface regions and to achieve a more

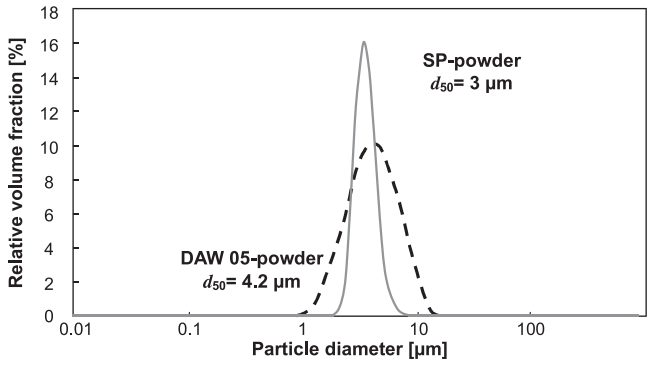

Fig. 2. Particle size distribution of spherical SP and DAW 05 alumina powders.

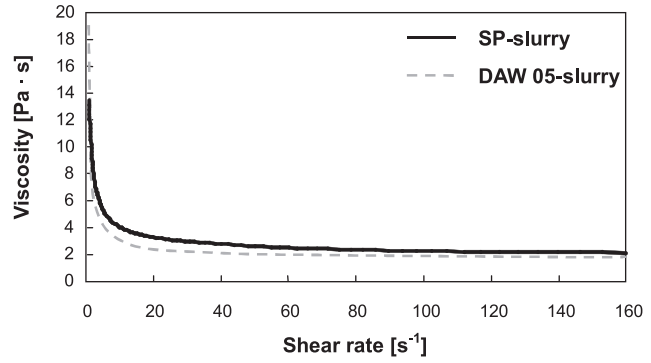

Fig. 3. Viscosity of SP- and DAW 05-slurries as a function of shear rate.

homogenous bulk-like setup for the sinter simulation. These systems are then subjected to free sintering until a density of around 85% is reached. For higher densities (i.e. over 90%) discrete element simulations of sintering are usually not applicable any more.[31] However, since the typical sintered densities reached in the accompanying experiments do not exceed ~75%, this simplification is quite adequate.

4. Results

4.1. Particle size and shape of powders

The particle size distribution curve derived by laser granulometry is shown in Fig. 2. The SP-powder exhibits a narrow distribution, while the DAW 05-powder shows a relatively broad particle size distribution. The viscosity of slurries as a function of shear rate is shown in Fig. 3. Both slurries show a shear thinning behavior and similar viscosity curves.

4.2. Properties of green and sintered tapes

After tape casting, the dried green sheets exhibit thicknesses of ~240 µm (SP-tape) and ~280 µm (DAW 05-tape), respectively, which relate to ~28% (SP-tape) and ~31% (DAW 05-tape) of the blade gap height of 900 µm. Fig. 4 shows the porosity change during the entire thermal treatment. In the green state both tapes exhibited a porosity of only ~5%. This highly dense structure of the green tapes is resulted from pore filling by the organic additives used. During thermal treatments these organic additives in the green tapes are burnt out. In the green state, both tapes contain ~40 vol.% organics including porosity. With increasing temperature, this value decreases significantly. Figs. 5 and 6 depict representative SEM micrographs taken from the ***xz***-cross section of both tapes after different thermal treatments. With increasing temperature the porosity decreases significantly; at the same time new sintering necks were formed. Visually, a significant difference in particle morphology of both alumina powders can be observed. The SP-powder exhibits a more uniform particle size, a pronounced spherical shape and a denser particle packing, which is in good accordance with lower tape thickness and porosity compared to DAW 05 as shown in Fig. 4.

4.3. Linear shrinkage and shrinkage anisotropy

Fig. 7 shows the linear shrinkage behavior after different steps of thermal treatment. After binder burnout (BBO), both tapes exhibit a lateral shrinkage <0.2%. In contrast, the BBO-shrinkage in the thickness direction is in value of ~2% and is much higher than the lateral BBO-shrinkage (Fig. 7). This extremely anisotropic shrinkage in the *z*-direction during binder removal was also observed by Patwardhanz and Cannon[13] and described in more detail for green tapes derived from powders of different particle shape by Fu and Roosen.[37] In these papers it is assumed that binder molecules and particles as well as pores will be oriented perpendicular to the *z*-direction, which results in higher *z*-shrinkage. In addition, it is considered that during binder burnout high adhesion forces occur between setter material and samples caused by melting of the binder.[37] Therefore, only *z*-shrinkage takes place. After pre-firing at 1600 °C for 1 h, the *z*-shrinkage of both tapes is slightly higher than the in-plane shrinkage, which is attributed to the high shrinkage in *z*-direction during binder burnout (Fig. 7). After sintering at 1600 °C for 10 h and 1730 °C for 5 h, respectively, the shrinkage in the *z*-direction is always smaller than the lateral shrinkage. After final sintering at 1730 °C for 15 h the linear shrinkages in all three spatial directions exhibit a nearly identical shrinkage value (Fig. 7). All these total shrinkage values consist of the shrinkage during BBO and sintering. After subtracting the BBO-shrinkage in the thickness direction of ~2%, the pure shrinkage during sintering in the thickness direction always exhibits lower values compared to that in the lateral directions (Fig. 7).

Fig. 8 shows the sintering shrinkage anisotropy factors ***K*** in all three spatial directions relative to the green tape geometry. It is noticeable that the shrinkage anisotropy factors $\boldsymbol{K_{xz}}$ and $\boldsymbol{K_{yz}}$ of both powders change significantly as a function of the thermal treatment whereas $\boldsymbol{K_{xy}}$ is constant with a value close to zero in both tapes and does not vary with temperature. I.e., during sintering at different temperatures, the ***x***- and ***y***-direction always exhibit the same amount of shrinkage. In contrast, the variation of the shrinkage values in the *z*-direction in dependence on thermal sintering treatments is more complex. After pre-firing at 1600 °C for 1 h, always positive ***K***-values were measured three-dimensionally in both tapes. But after sintering at 1600 °C for 10 h and 1730 °C for 5 h, the sign of $\boldsymbol{K_{xz}}$ and $\boldsymbol{K_{yz}}$ becomes

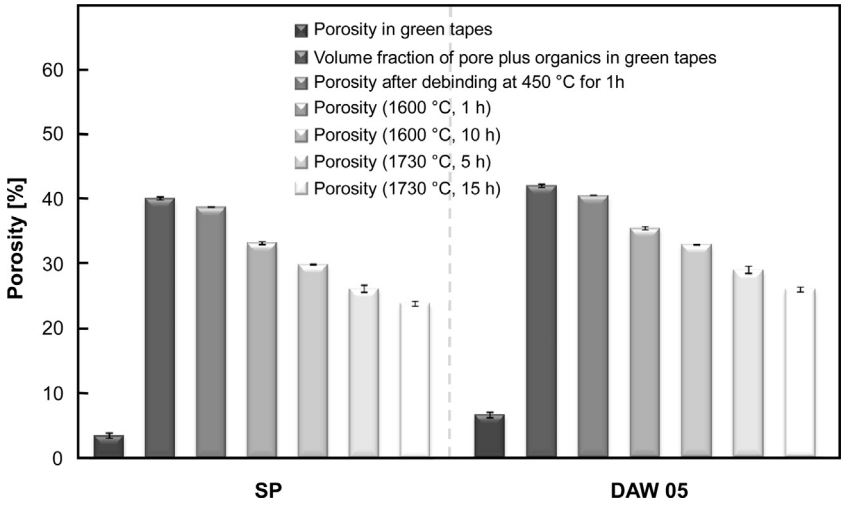

Fig. 4. Porosity in green tapes and in tapes after thermal treatment at different temperatures.

negative, indicating a lower z-shrinkage (Fig. 8), which will be further discussed in Section 4.5. During sintering at 1730 °C with 15 h dwell time, a higher shrinkage rate occurs in z-direction and after that thermal treatment the three $\boldsymbol{K}$-values lie again very close to each other (Fig. 8).

Because of the high z-BBO-shrinkage the shrinkage anisotropy factors $\boldsymbol{K}'$ were also calculated after subtracting the BBO-strain. These $\boldsymbol{K}'$-factors relative to the geometry of the debinded tape are shown in Fig. 9 in dependence on different thermal sintering treatments. After subtracting the strains

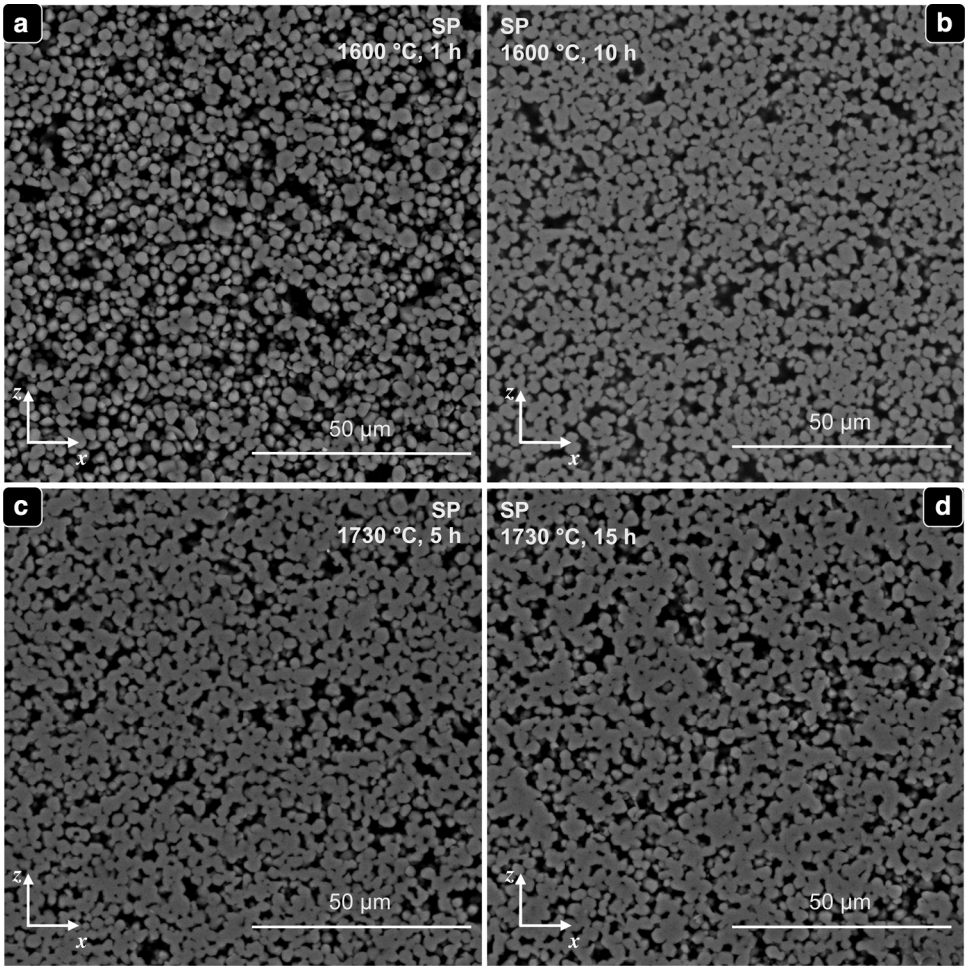

Fig. 5. Representative SEM micrographs of xz-cross sections of SP alumina tapes at different temperatures.

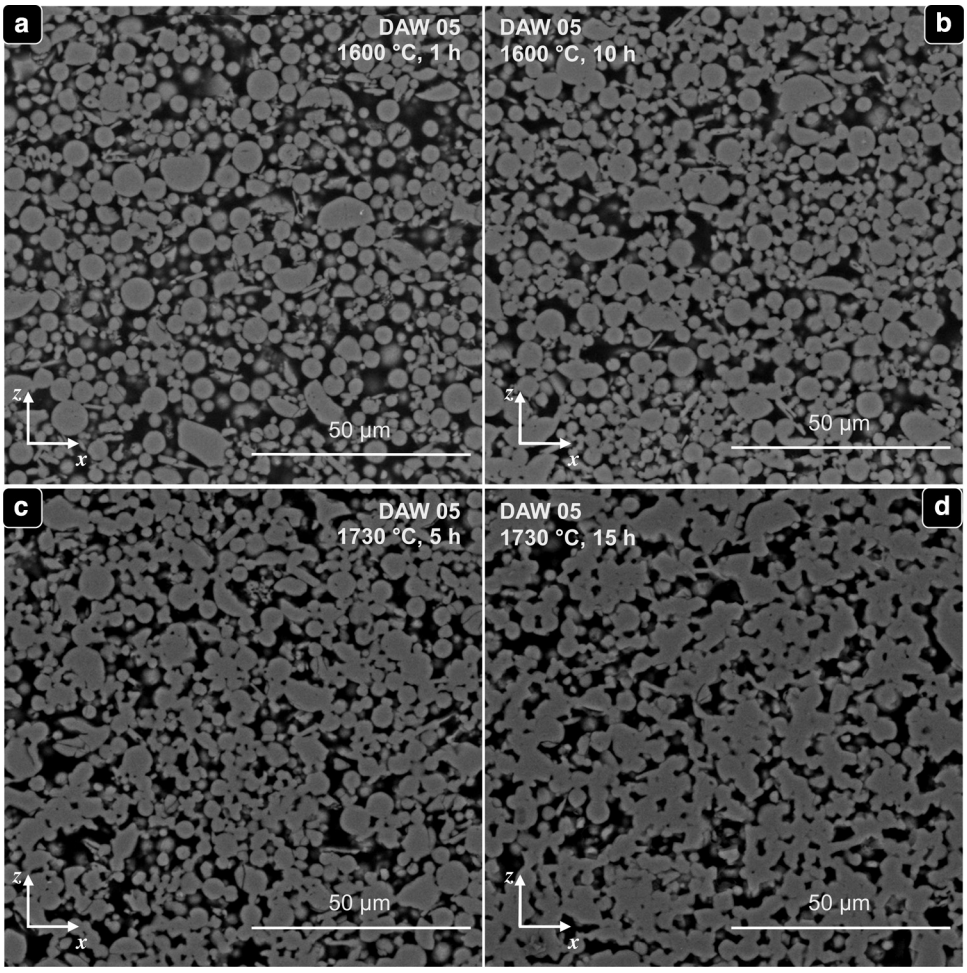

Fig. 6. Representative SEM micrographs of xz-cross sections of DAW 05 alumina tapes at different temperatures.

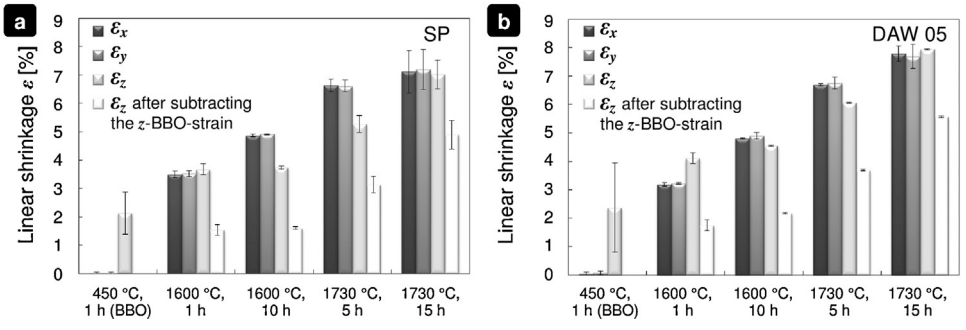

Fig. 7. Linear shrinkage of (a) SP- and (b) DAW 05-tapes after different thermal treatments.

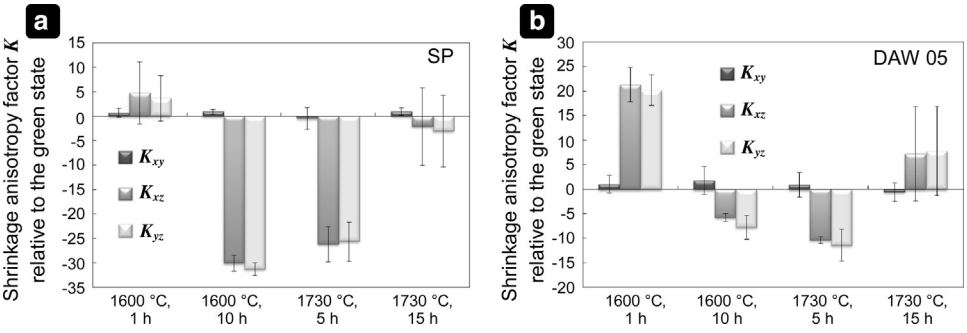

Fig. 8. (a) and (b) Shrinkage anisotropic factors $\boldsymbol{K}$ relative to the green state of SP- and DAW 05-tapes in all three spatial planes after different thermal sintering treatments.

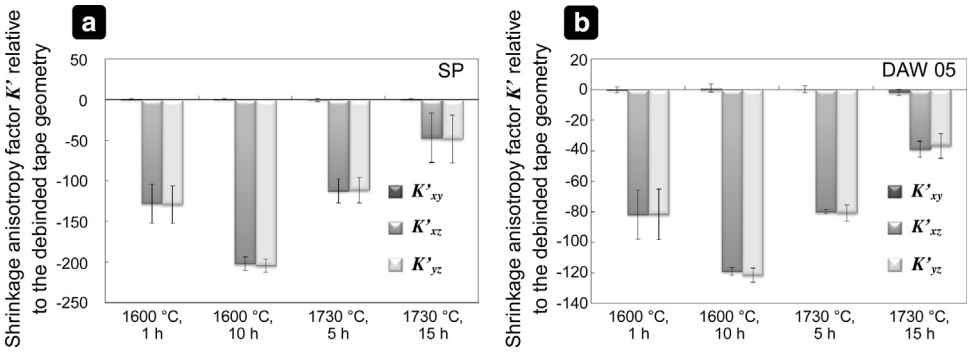

Fig. 9. (a) and (b) Shrinkage anisotropic factors K' relative to the debinded tape geometry, i.e. for the calculation of K' the BBO-strain of SP- and DAW 05-tapes was substracted from the total sintering shrinkage in all three spatial planes after different thermal sintering treatments.

occurring during binder burnout, the lateral directions still exhibit the same shrinkage at different temperature treatments with K'_{xy} of ~0, whereas the K'_{xz}- and K'_{yz}-values always lie under the K'_{xy}-data (Fig. 9), indicating a lower residual sintering shrinkage in the z-direction than that in the lateral directions. With increasing temperature, K'_{xz} and K'_{yz} approach to zero, i.e., a more isotropic shrinkage behavior was observed at higher temperature.

To summarize, during the whole thermal treatment process of green tapes derived from spherical powders, the x- and y-direction always exhibit the same shrinkage with K_{xy} of ~0. But the variation of the shrinkage rate in the z-direction is very complicated in dependence on thermal treatment at different temperatures. At the beginning of thermal treatment the main reason of the shrinkage anisotropy in the z-direction is the high strain in the z-direction during binder removal. During further thermal treatments the complex shrinkage behavior in the z-direction is explained by pore orientation and by the difference in the coordination number in different directions induced by particle rearrangement, which will be discussed in detail in Section 4.5.

4.4. Microstructure analysis

According to the methods described in Section 2.5 the pore orientation was analyzed in all three spatial planes pixel by pixel. The porosity P measured by image analysis (see Table 2) is in good agreement with the values P_{bulk} derived from the density measurements shown in Fig. 4. During the entire thermal process the pore orientation factor S in all three spatial planes is positive for both powders (see Table 2), i.e., the pores are always aligned perpendicular to the z-direction despite the spherical particle shape. In the SP-tape manufactured from more regular spherical particles, the three S-values in the three spatial planes are similar to each other and close to zero. In the SP-tape, the main cause of the shrinkage anisotropy is the BBO-shrinkage in the thickness direction,[13,37] which also results in particle rearrangement. In the DAW 05-tape, which exhibits a less regular particle shape, its S_{xy}-value is always slightly lower than the corresponding S_{xz}- and S_{yz}-values. I.e., with increasing particle shape anisotropy, pores will be more strongly aligned perpendicular to the thickness direction. This pore orientation in green tapes based on spherical particles is caused by constrained drying and binder burnout effects; during drying the shrinkage can only be carried out in z-direction due to the adhesion forces between slurry and carrier tape; during binder burnout the shrinkage also occurs only in the thickness direction as shown in Fig. 7 and will be discussed in Section 5.

4.5. Numerical analysis

In the following, the simulation results for all three processing steps are described.

4.5.1. Tape casting simulation

The initial simulation setups were generated by randomly inserting particles in the simulation cell while ensuring that there is no overlap between two particles. Six setups for the ESP powder and six for the PSD powder were made. As mentioned in Section 3.1, the systems were sheared for 0.18 s. The coordination number of the particles in the system is calculated before and after the simulation and analyzed in all directions to investigate the influence of the shear field on the particle ordering. As each set of simulation consists of six different setups with the same powder (ESP or PSD) and the same shear history or its absence, respectively, the results are averaged over those six simulations resulting in four sets of data.

Before shear is applied, the particles have a coordination number close to zero in all directions. The application of the shear field increases the total coordination number for all setups, being slightly smaller in the case of ESP where it is 0.695 compared to 0.753 for PSD. If the individual directions are taken into account, the coordination number is marginally higher in x- and z-direction than in the y-direction. In the case of ESP, the coordination numbers in x-, y- and z-directions are 0.218, 0.179 and 0.297, respectively. For PSD they are 0.281, 0.194 and 0.277. Neither for ESP nor for PSD a strong ordering of the particles can be seen at the end of the tape casting simulation.

4.5.2. Drying simulation

The input particle arrangements for the drying simulations are the initial setups prior to the tape-casting stage for the non-sheared systems and the outcome of the tape-casting simulations for the sheared systems. As in the previous section,

Table 2
Pore orientation S and porosity P in microstructure measured by image analysis.

SP-powder	S_{xy} *	S_{xz} *	S_{yz} *	P_{bulk} ** [%]	P_{xy} *** [%]	P_{xz} *** [%]	P_{yz} *** [%]
1600 °C, 1 h	2.31 ± 0.21	2.59 ± 0.29	1.77 ± 0.75	33.2 ± 0.2	39.5 ± 0.8	33.2 ± 0.6	34.5 ± 1.2
1600 °C, 10 h	1.55 ± 0.54	2.78 ± 0.63	1.71 ± 0.17	30.0 ± 0.1	33.8 ± 1.0	28.7 ± 0.8	28.4 ± 0.7
1730 °C, 5 h	1.17 ± 0.93	2.76 ± 1.10	2.54 ± 0.96	26.2 ± 0.6	30.6 ± 0.7	26.4 ± 1.1	27.1 ± 1.2
1730 °C, 15 h	2.12 ± 0.73	2.42 ± 0.76	2.06 ± 0.70	23.9 ± 0.8	26.7 ± 1.7	25.1 ± 0.9	20.8 ± 3.6
DAW 05-powder	S_{xy} *	S_{xz} *	S_{yz} *	P_{bulk} ** [%]	P_{xy} *** [%]	P_{xz} *** [%]	P_{yz} *** [%]
1600 °C, 1 h	3.06 ± 0.51	5.36 ± 0.47	5.77 ± 0.94	35.4 ± 0.2	42.1 ± 1.2	39.1 ± 1.7	41.6 ± 2.2
1600 °C, 10 h	1.06 ± 0.63	5.57 ± 1.22	6.16 ± 0.76	32.9 ± 0.1	39.0 ± 1.1	32.0 ± 0.6	32.4 ± 0.9
1730 °C, 5 h	3.60 ± 1.02	5.50 ± 2.12	5.54 ± 0.28	29.0 ± 0.2	33.8 ± 0.9	29.9 ± 2.8	30.8 ± 1.1
1730 °C, 15 h	3.65 ± 1.18	4.43 ± 1.66	5.21 ± 0.68	26.0 ± 0.5	32.6 ± 1.6	28.6 ± 2.3	31.6 ± 0.4

* S: pore orientation factor calculated by modified linear intercept method (Section 2.5.1).
** P_{bulk}: total porosity in bulk volume measured geometrically (Section 2.3).
*** P: porosity measured by image analysis.

the coordination number both in total and in all three spatial directions is analyzed during the drying process to investigate the influence of this process on the particle ordering. As before, the results are averaged over the six setups of each system resulting in four sets of data.

As shown in Fig. 10 the initial coordination number in the three directions has no influence on the final packing state of both powder systems. The final coordination number is ~6% higher in systems with the ESP powder. These systems have a final coordination number of 6.06 for the non-sheared starting setup and 6.07 for the setup subjected to a preceding tape cast (shear) simulation. For the systems with PSD the coordination numbers are 5.72 and 5.71, respectively. Fig. 10 indicates that the difference between the coordination number in the z-direction and in the other two directions is slightly higher in the case of the sheared setups. Taking into account that the difference between the sheared and non-sheared results is in the range of the statistical variance, it can be concluded that the final total coordination number depends on the particle size distribution but not significantly on the shear history for the systems used in this study. Yet, if the directions are taken into account the influence of the shear history is slightly visible.

The volume fraction of the ceramic particles after the drying simulation is around 62%. This is close to the experimental results for the SP- and the DAW 05-powders which, after drying and BBO, show a volume fraction between 64% and 67% (Fig. 4).

4.5.3. Sintering simulation

As input for the final sintering simulations the resulting particle positions from the drying simulations are used. Again, the results are averaged over the six setups of each system resulting in four sets of data. The shrinkage anisotropy factors K are calculated over the duration of the simulation. The shrinkage and shrinkage rates in the three main directions are calculated by evaluating the displacement of the particles during the simulation in relation to their initial positions. Additionally, the coordination number in each direction is tracked over the sintering time.

The simulated shrinkage anisotropy factor K at a density of 85% after firing (Fig. 11) shows a behavior which is qualitatively similar to the experiment, albeit not as pronounced. Both, the sheared and the non-sheared ESP systems have a K_{xy} value of almost 0 and negative K_{xz} and K_{yz} values in accordance to the experimental data. The sheared systems exhibit a slightly higher anisotropy in z-direction compared to the system which was only dried. The non-sheared system with ESP shows, compared to the other systems, the least scatter, whereas the same systems have a bigger standard deviation after being sheared. The systems with PSD have a larger scattering around the mean K value than the system with ESP, which is most probably due to the larger influence of the randomized initial particle sizes on the packing behavior. For the non-sheared systems the behavior is similar to the experiment (i.e. K_{xy} near 0) for both ESP and PSD. In the case of the sheared systems the scattering becomes more pronounced. Nevertheless, the general trend of the K_{xz} and K_{yz} values being smaller than K_{xy} is true for all systems, and is in good agreement with experimental results as shown in Fig. 9.

To obtain a better understanding of what happens during the sintering process, the contacts between the particles were determined over time in all three directions (Fig. 12); based on these initial particle contacts, sintering necks will be formed during thermal treatment. The coordination numbers calculated for the initial stage of the sintering simulations differ slightly from those shown in Fig. 10 for the final drying stage due to the aforementioned cropping of the setup before sintering. All systems start with the highest coordination number in z-direction and slightly lower, but equal coordination numbers in the two remaining directions. During densification new contacts are formed at a higher rate in x- and y-direction than in z-direction resulting in an almost equal coordination number in all three directions at the final density of 85%. This agrees well with the shrinkage anisotropy factors shown in Fig. 11. Compared to the non-sheared systems, the sheared systems show a larger difference between the coordination numbers in z-direction on the one hand and the coordination numbers in x- and y-direction on the other hand. This result is again in accordance with the higher K_{xz} and K_{yz} values in the sheared systems.

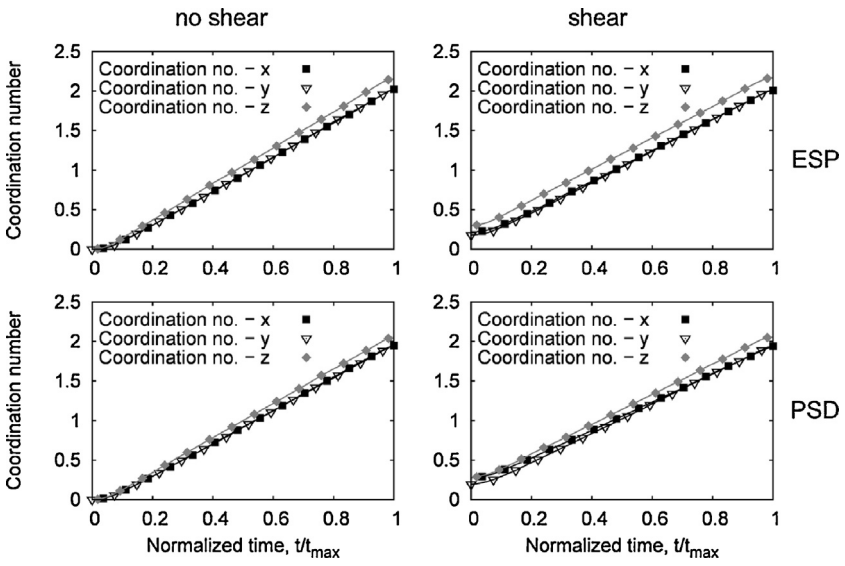

Fig. 10. Coordination number in the spatial directions as a function of the time during drying.

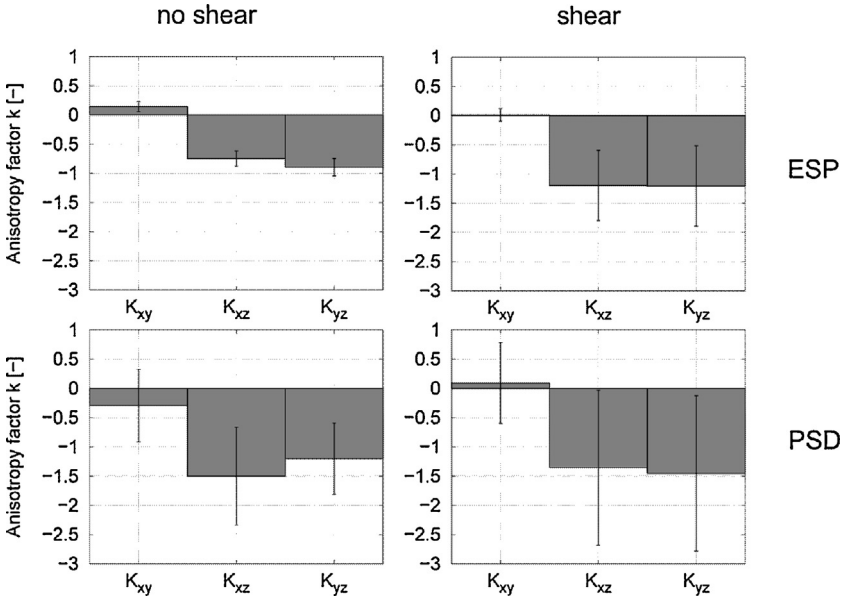

Fig. 11. Anisotropy factor $\boldsymbol{K}$ after sintering at a density of 85%.

5. Discussion

Experimentally, two different spherical powders were used for tape casting. During drying and binder burnout the shrinkage of the tapes occurs almost only in the z-direction due to adhesion forces of the cast tape on the carrier film and of the dried tape on the setter material. During sintering $\boldsymbol{K_{xy}}$ stays always constant with a value close to zero, while the $\boldsymbol{K_{xz}}$ and $\boldsymbol{K_{yz}}$ values are always lower. The variation of $\boldsymbol{K_{xz}}$ and $\boldsymbol{K_{yz}}$ during thermal treatments is relatively complicated due to pore orientation and different coordination numbers in different directions induced by particle rearrangement. In initial sintering stages, the shrinkage anisotropy in the z-direction is caused by high z-BBO-shrinkage. After subtracting the BBO-shrinkage from the total shrinkage, the z-direction always exhibits a lower shrinkage than that in lateral directions. With increasing temperature the shrinkage in all three spatial directions approaches to each other and the shrinkage anisotropy decreases. Due to different particle shape and particle size distribution, the DAW 05- and SP-tapes also show different anisotropic shrinkage behavior in the thickness direction. The cast green tapes exhibit an anisotropic microstructure, where the pores show an anisotropic structure with an orientation normal to the thickness direction (Table 2). The observation of a smaller z-shrinkage compared to the lateral shrinkage is opposite to literature data as reported in former publications.[8,13,14,16] The reason for the discrepancy is the consideration of the BBO-Shrinkage, which was determined in all three spatial directions in the present study, while other papers always measured the total shrinkage and the impact of binder burnout was disregarded. Furthermore, in the present

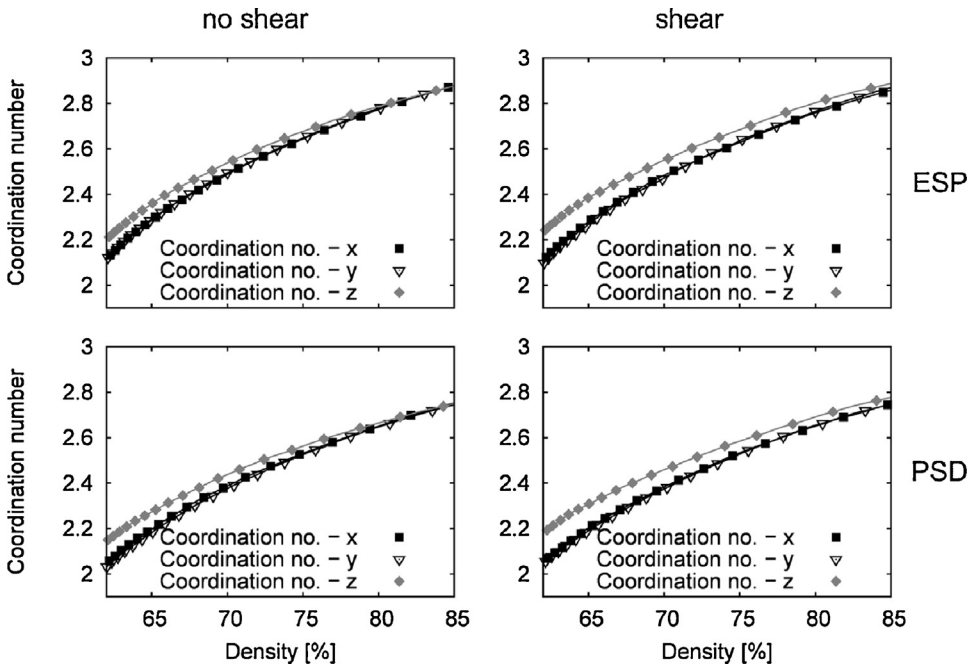

Fig. 12. Coordination number as a function of the relative density during sintering.

study almost spherical particles were investigated for tape casting, while other papers used non-spherical particles like, e.g., milled powders. For such tapes derived from non-spherical particles, always a higher z-shrinkage compared to the lateral shrinkage was observed[13,14,16] and in this case their sintering behavior can be described based on the model of Olevsky.[16,24,22]

It is noticeable that the experimentally observed anisotropy in Fig. 9 is about 100 times higher than the anisotropy calculated numerically (Fig. 11). This is partly based on the definition of the anisotropy factor used, which magnifies small differences (see Eqs. (2)–(4)). The other possible reasons for the large difference are discussed below. However, since the aim of the simulation is to get a better understanding of the mechanisms occurring, these quantitative differences should not be overvalued. Qualitatively the general trend both in simulation and experiment is similar: The anisotropy decreases with sintering time and a lower shrinkage in the thickness direction was observed in both cases. Further differences between simulation and experiment result from the fact that two idealized fully spherical powders were used in the simulations and, additionally, due to the simplifications made in the models used in the numerical study along the process chain. One cause of deviation could be the assumption of a Couette flow under the blade, whereas a Couette flow overlapping with a pressure driven Poiseuille flow would be more appropriate. However, due to the low fill height of the slurry in the reservoir and the high casting velocity the influence of the hydrostatic pressure should be almost negligible. Presumably of more importance is, therefore, the fact that the binder is not explicitly modeled in the simulation. This simplification makes it impossible to investigate the formation of binder layers and their influence on particle ordering in the simulation as detailed further down.

Another simplification is probably less significant: the drying simulations only describe the constant-rate period of the drying process. The falling-rate period is not simulated and could lead to an additional particle rearrangement in the real process, which is not taken into account in the simulation. As these rearrangements should be small compared to the particle movements during the first drying stage, however, their influence on the final particle ordering should be small.

Furthermore, the horizontal capillary forces during drying were not used in the simulation, so that the shrinkage occurs only in the z-direction; higher z-coordination numbers were measured after drying. In the experiments the bottom side of the wet ceramic film during drying is constrained due to adhesion forces between ceramic tape and the carrier tape, which only allows a drying shrinkage in the thickness direction. But actually, the capillary forces in horizontal direction still exist in reality, which could pull particles laterally together and lead to some further particle rearrangement. In the experiments some lateral camber of dried ceramic tape can be often observed due to these horizontal capillary forces. The consequence of this omission is hard to specify and, therefore, could significantly contribute to the observed discrepancy between model prediction and experimental observation.

The potentially most important difference between the simulation and the experiment is the absence of the BBO in the modeling. During the BBO the binder will become liquid and through the formation of liquid bridges between the ceramic particles, which can exert significant forces on them, a rearrangement of said particles will certainly occur to some degree. Additionally, the gasification of the binder creates a network of pores leading to stresses in the structure. Due to the fact that this stage of the process is not simulated the particle packing used in the sintering simulation should differ from the

one emerging from the BBO in reality. Unfortunately, considering these mechanisms would require a totally new simulation model with the possibility of simulating processes at a significant smaller scale than the models used in this study. Due to high computational cost such a model would prevent the simulation of a large amount of particles and would, therefore, be difficult to get coupled into the simulation scheme used in this work.

The experimentally derived pore orientation factor $\boldsymbol{S}$ (in Table 2) does not show a clear trend with increasing temperature in both tapes. Wakai and Guillon[41] observed considerable pore rounding from the initial sintering stage to the final stage in a SiO_2–Na_2O–CaO–MgO–Glass film. This pore rounding effect was not observed in the current experimental study; after firing at 1730 °C a residual porosity of ~25% still remains in both tapes. That is, the pore shape variation between initial and intermediate sintering period is not significant. Exner and Giess[39] studied the pore shape evolution and the shrinkage anisotropy variation in dependence on sintering temperature for the final sintering stage of a cordierite-type glass. The direction-dependent shrinkage becomes more isotropic at higher temperatures, while the pore shape does not show significant changes.[39] Boccaccini and Trusty pointed out, that compared to the pore orientation and particle arrangement in the microstructure, the contact information between neighboring particles plays a more important role for the varying shrinkage anisotropy.[40] However this contact information is difficult to obtain experimentally; except from complex procedures like electron synchrotron microtomography.[35] In the present study, as mentioned above, the binder removal has great influence on shrinkage in the thickness direction and particle rearrangement, but was not taken into account for the simulation. Therefore, the numerically derived coordination number does not predict the experimentally observed pore orientation evolution at different temperatures, but it is very important for the varying shrinkage anisotropy. In addition the numerically derived coordination number exhibits only small, but clear differences in the three spatial directions, which are not detected in the experiment.

Nevertheless, the simulations still exhibit the main experimental characteristics and are therefore valuable in getting additional insight. In the simulations the smallest shrinkage is predicted in the thickness direction. This is the case even though the coordination number in this direction is the highest at the onset of the sintering process. The number of contacts in the lateral directions is only marginally smaller, which means that sintering activity will also take place in those directions. Due to the small distance between neighboring particles at a volume fraction slightly above 60% new contacts should be formed quite quickly. More free space between the particles exists in the lateral directions as the initial coordination number in those directions is smaller. This should allow for a larger number of potential new contacts in those directions than in the thickness direction. As these new contacts have a higher sintering force due to the lower contact area the shrinkage rate in the lateral directions should be higher than in the thickness direction. Therefore, the coordination numbers of all directions are converging over time, as can be seen in Fig. 12.

Generally speaking, the shrinkage rate of the system is the highest in the direction where the particles encounter the lowest resistance, i.e. the lowest contact area. This leads to a more homogenous density distribution and a more isotropic microstructure over sintering time as observed also by others in both hot forging experiments and simulations of alumina.[35,38]

In the present paper, this effect is even more pronounced for systems which have been sheared prior to being dried. In accordance to the afore-mentioned theory this behavior can be explained by the fact that the anisotropy of the coordination number is higher in sheared systems than in non-sheared systems.

6. Conclusions

The shrinkage behavior of cast green tapes composed of spherical particles was investigated three-dimensionally during binder burnout (BBO) and sintering. During BBO the z-shrinkage is approximately ten times higher than the in-plane shrinkage, because this is a constrained densification process and shrinkage can only occur perpendicular to the casting plane. After subtracting the BBO-shrinkage, the lateral directions (x- and y-directions) always exhibit the same shrinkage during sintering at different temperatures and holding times with a $\boldsymbol{K'}_{xy}$ of ~0, while $\boldsymbol{K'}_{xz}$ and $\boldsymbol{K'}_{yz}$ are negative and approach to zero with increasing temperature. The microstructural analysis shows pore orientation perpendicular to the thickness direction.

The simulations show a similar behavior which agree qualitatively well with the experimental data. Due to some necessary simplifications in the numerical model it is not possible to achieve a full quantitative agreement. The influence of the tape casting process (i.e. the shear field under the blade) on the particle ordering in a system consisting of spherical particles is visible in the later processing steps. Especially the particle ordering caused by tape casting persists after the drying stage and has a small impact on the sintering behavior. This behavior is observable for systems with equally sized particles (ESP) as well as for systems with a particles size distribution (PSD). In summary, it can be stated that the simulation is in accordance with the experimental finding that anisotropic shrinkage occurs already in tape-cast sheets made from slurries with spherical ceramic particles.

Acknowledgments

Financial support from the German Research Foundation (Deutsche Forschungsgemeinschaft, Bonn, Germany) under the contracts of KR1729/9 and RO653/12 is gratefully acknowledged. Furthermore, the authors wish to thank Tobias Rasp from the Fraunhofer IWM, Freiburg, Germany for fruitful discussions concerning the DEM sintering model.

References

1. Raj PM, Odulena A, Cannon WR. Anisotropic shrinkage during sintering of particle-oriented systems—numerical simulation and experimental studies. *Acta Mater* 2002;**50**(1):2559–70.

2. Roosen A. Tape casting. In: Riedel R, Chen IW, editors. *Ceramics science and technology: synthesis and processing*. Weinheim: Wiley-VCH Verlag GmbH; 2012. p. 39–62.
3. Pohle D, Wagner M, Roosen A. Effect of friction on inhomogeneous shrinkage behavior of structured LTCC tapes. *J Am Ceram Soc* 2006;**89**(9):2731–7.
4. Jean JH, Chang CR. Effect of densification mismatch on camber development during co-firing of nickel-based multilayer ceramic capacitors. *J Am Ceram Soc* 1997;**80**(9):2401–6.
5. Imanaka Y, Kamehara N. Influence of shrinkage missmatch between copper and ceramics on dimensional control of the multilayer ceramic circuit board. *J Ceram Soc Jpn* 1992;**100**(4):560–4.
6. Sawhill HT, Jensen RH, Mikeska KR. Dimensional control in low-temperature co-fired ceramic multilayers. *Ceram Trans* 1989;**15**:611–28.
7. Besendörfer G, Roosen A. Particle shape and size effects on anisotropic shrinkage in tape-cast ceramic layers. *J Am Ceram Soc* 2008;**91**(8):2514–20.
8. Heunisch A, Dellert A, Roosen A. Effect of powder, binder and process parameters on anisotropic shrinkage in tape cast ceramic products. *J Eur Ceram Soc* 2010;**30**:3397–406.
9. Wonisch A, Polfer P, Kraft T, Dellert A, Heunisch A, Roosen A. A comprehensive simulation scheme for tape casting: from flow behavior to anisotropy development. *J Am Ceram Soc* 2011;**94**(7):2053–60.
10. Wu M, Messing GL. Fabrication of oriented SiC-whisker-reinforced mullite matrix composites by tape casting. *J Am Ceram Soc* 1994;**77**(10):2586–92.
11. Ozer IO, Suvaci E, Karademir B, Missiaen JM, Carry CP, Bouvard D. Anisotropic sintering shrinkage in alumina ceramics containing oriented platelets. *J Am Ceram Soc* 2006;**89**(6):1972–6.
12. Watanabe H, Kimura T, Yamaguchi T. Particle orientation during tape-casting in the fabrication of the grain-oriented bismuth titanate. *J Am Ceram Soc* 1989;**72**(2):289–93.
13. Patwardhanz JS, Cannon WR. Factors influencing anisotropic sintering shrinkage in tape-cast alumina: effect of processing variables. *J Am Ceram Soc* 2006;**89**(10):3019–26.
14. Greenwood R, Roncari E, Galassi C. Preparation of concentrated aqueous alumina suspensions for tape casting. *J Eur Ceram Soc* 1997;**17**(12):1393–401.
15. Raj PM, Cannon WR. Anisotropic shrinkage in tape-cast alumina: role of processing parameters and particle shape. *J Am Ceram Soc* 1999;**82**(10):2619–25.
16. Fu Z, Dellert A, Roosen A. Effect of pore orientation on anisotropic shrinkage in tape-cast products. *J Eur Ceram Soc* 2014;**34**(10):2483–95.
17. Zhu X, Sakka Y. Textured silicon nitride: processing and anisotropic properties. *Sci Technol Adv Mater* 2008;**9**(3):1–47.
18. Zhang W, Melcher R, Travitzky N, Bordia RK, Greil P. Three-dimensional printing of complex shaped alumina/glass composites. *Adv Eng Mater* 2009;**11**(12):1039–43.
19. Travitzky N, Windsheimer H, Fey T, Greil P. Preceramic paper-derived ceramics (feature). *J Am Ceram Soc* 2008;**91**:3477–92.
20. Ch'ng HN, Pan J. Modelling microstructural evolution of porous polycrystalline materials and a numerical study of anisotropic sintering. *J Comput Phys* 2005;**204**(2):430–61.
21. Olevsky EA, Skorohod V. Deformation aspects of anisotropic porous bodies sintering. *J Phys IV* 1993;**3**:739–42.
22. Olevsky EA, Kushnarev B, Maximenko AL, Tikare V. Sintering of oriented pore–grain structures. *Ceram Trans* 2012;**157**:35–40.
23. Zavaliangos A, Missiaen JM, Bouvard D. Anisotropy in shrinkage during sintering. *Sci Sintering* 2006;**38**:13–25.
24. Tikare V, Braginsky M, Olevsky E, Johnson DL. Numerical simulation of anisotropic shrinkage in a 2D compact of elongated particles. *J Am Ceram Soc* 2005;**88**(1):59–65.
25. Olevsky E, Kushnarev B, Maximenko A, Tikare V, Braginsky M. Modelling of anisotropic sintering in crystalline ceramics. *Philos Mag* 2005;**85**(19):2123–46.
26. Wakai F, Chihara K, Yoshida M. Anisotropic shrinkage induced by particle rearrangement in sintering. *Acta Mater* 2007;**55**(13):4553–66.
27. Salmang H, Scholze H. *Keramik*. 7th ed. Berlin: Springer-Verlag; 2007.
28. Underwood EE. *Quantitative stereology*. Reading, MA: Addison-Wesley; 1970.
29. Cundall PA, Strack ODL. A discrete numerical model for granular shear assemblies. *Geotechnique* 1979;**24**(4):411–26.
30. Fujita M, Yamaguchi Y. Development of three-dimensional structure formation simulator of colloidal nanoparticles during drying. *J Chem Eng Jpn* 2006;**39**(1):83–9.
31. Henrich B, Wonisch A, Kraft T, Moseler M, Riedel H. Simulations of the influence of rearrangement during sintering. *Acta Mater* 2007;**55**:753–62.
32. Allen MP, Tildesley DJ. *Computer simulations of liquids*. New York, NY: Oxford University Press; 1997.
33. Breinlinger T, Kraft T. A simple method for simulating the coffee stain effect. *Powder Technol* 2014;**256**:279–84.
34. Scherer GW. Theory of drying. *J Am Ceram Soc* 1999;**73**(1):3–14.
35. Wonisch A, Guillon O, Kraft T, Moseler M, Riedel H. Stress-induced anisotropy of sintering alumina: discrete element modelling and experiments. *Acta Mater* 2007;**55**:5187–99.
36. Rasp T, Jamin C, Wonisch A, Kraft T, Guillon O. Shape distortion and delamination during constrained sintering of ceramic stripes: discrete element simulations and experiments. *J Am Ceram Soc* 2012;**95**(2):586–92.
37. Fu Z, Roosen A. Shrinkage of tape cast products during binder burnout. *J Am Ceram Soc* 2014;**98**(1):20–9.
38. Zuo R, Aulbach E, Bordia RK, Rödel J. Critical evaluation of hot forging experiments: case study in alumina. *J Am Ceram Soc* 2003;**86**(7):1099–105.
39. Exner HE, Giess EA. Anisotropic shrinkage of cordierite-type glass powder cylindrical compacts. *J Mater Res* 1988;**3**(1):122–5.
40. Boccaccini AR, Trusty PA. In situ characterization of the shrinkage behavior of ceramic powder compacts during sintering by using heating microscopy. *Mater Charact* 1998;**41**:109–21.
41. Wakai F, Guillon O. Evaluation of sintering stress from 3-D visualization of microstructure: case study of glass films sintered by viscous flow and imaged by X-ray microtomography. *Acta Mater* 2014;**66**:54–62.